Philosophical Magazine Letters
Vol. 00, No. 00, January 2010, 1–17

Shearing of γ' precipitates in Ni-base superalloys: A phase field study incorporating the effective γ-surface

V.A. Vorontsov[a*], R.E. Voskoboinikov[b]

and C.M.F. Rae [c]

[a]*Department of Materials, Imperial College London, South Kensington Campus, London, UK, SW7 2AZ*; [b]*Institute of Materials Engineering, ANSTO, New Illawarra Road, Lucas Heights, NSW, Australia;* [c]Department of Materials Science and Metallurgy, University of Cambridge, Pembroke Street, Cambridge, UK, CB2 3QZ

(*Received on ..*)

An extended Phase Field Model of Dislocations in Ni-base superalloys is presented. It incorporates the recently developed effective γ-surfaces for both matrix and precipitate phases, obtained from atomistic simulations. These novel γ-surfaces feature extrinsic stacking faults as additional local minima. Thus, they offer an increased number of available dislocation dissociation pathways within the phase field system. The new model has been used to simulate a variety of mechanisms for γ' precipitate shearing proposed in literature. A critical assessment is made based on the modelling observations.

Keywords: Primary creep; dislocation dissociation; phase field model of dislocations; Shockley partials; extrinsic stacking faults.

1. Introduction

In a preceding work, Vorontsov *et al.* [1] used the Phase Field Model of Dislocations (PFMD) [2] to investigate the shearing of γ' precipitates in Ni-base superalloys under primary creep conditions (750-850 °C and $\sigma_{[001]}$>500 MPa) [3]. The study concentrated on the phenomenon of stacking fault shear, where the $L1_2$ ordered precipitates are cut by $a\langle 112\rangle$ dislocations. TEM observations [3] have shown that these dislocations are able to penetrate the γ' precipitates by dissociating into partial dislocations separated by widely extended low-energy superlattice intrinsic and extrinsic stacking faults (SISF and SESF respectively).

Using PFMD, it was found [1] that the shearing of γ' precipitates was sensitive to the shape of the precipitate, the difference in resolved stresses experienced by the constituent dislocations of the $a\langle 112\rangle$ ribbon and the overall magnitude of the applied stress. However, the experimentally observed formation of the SESF was not incorporated into the physics of the model used in [1]. In this paper, we extend the model to accurately reproduce the extrinsic faults. Using this more realistic representation of the energy of a generalised stacking fault (GSF) during crystal shearing, we examine the stability of various combinations of dislocations passing through the γ matrix and the γ' precipitates and discuss this in relation to the governing mechanisms and experimental observations in deformed Ni-base superalloys.

*Corresponding author. Email: vassili.vorontsov@googlemail.com

ISSN: 0950-0839 print/ISSN 1362-3036 online

DOI: 10.1080/09500839.20xx.xxxxxx
http://www.informaworld.com

In PFMD, the crystal free energy term, F_{crystal}, defines the periodic misfit potential associated with the lattice disregistry due to a shear displacement in the crystal. The formulation of F_{crystal} allows the incorporation GSF energy, also known as a γ-surface, obtained from atomistic simulations [4, 5] such as Density Functional Theory (DFT) or the Embedded Atom Method (EAM). The topography of the surface determines the dislocation core structure in the phase field simulations. This includes dissociation into partial dislocations accompanied by the formation of stacking faults and anti-phase boundaries (APBs).

The γ-surfaces [6] used for the matrix and precipitate phases in the earlier study [1] incorporate atomic displacements in one crystallographic plane only. As a result, they cannot reflect the existence of any kind of extrinsic stacking fault and/or microtwins and are consequently unsuitable for modelling dislocation driven deformation processes that involve formation of extrinsic faults. Employment of a principally new type of γ-surface is required in order to address this issue.

The study is presented in the following manner. A brief description of the computational procedure for evaluation of the effective γ-surfaces is provided in Section 2. The framework of the PFMD model implemented in this research is given in Section 3. Here we also disclose the fitting of the effective γ-surfaces obtained in [7] to the PFMD model as well as the reformulation of the γ-surfaces in terms of the order parameters η_i where $i = 1,\ldots,3$. A thorough discussion of the obtained results of PFMD modelling of an isolated γ' precipitate shear by an $a\langle 112\rangle$ dislocation, a pair of $\frac{a}{3}\langle 112\rangle$, a pair of identical $\frac{a}{2}\langle 110\rangle$ dislocations and a single $\frac{a}{2}\langle 110\rangle$ dislocation is conducted in Section 4. Finally, conclusions are drawn in Section 5.

2. Background

Typically, γ-surfaces are calculated using the original approach introduced by Vitek in 1968 [8]. In this method, two half-crystals are displaced relative to one another. The energy density, γ, associated with each displacement, (ξ, ζ), is evaluated and used to map out a surface that reflects the periodicity and symmetry of the crystal.

$$\gamma\left(\xi,\zeta\right) = \Delta E\left(\xi,\zeta\right) = E\left(y+\xi, z+\zeta\right) - E\left(y,z\right) \tag{1}$$

Following Frank [9], one can conclude that only intrinsic stacking faults can be taken into consideration using [8].

Voskoboinikov and Rae [7] extended this method to produce an effective γ-surface in the $\{111\}$ crystallographic plane that self-consistently incorporates both intrinsic and extrinsic stacking faults. In this modification, an additional floating plane is introduced between the two half-crystals. For every displacement of the half-crystals, the position of the middle plane is adjusted in order to obtain the minimum possible energy density. For the (111) plane in Ni_3Al, the effective γ-surface is defined in the following equation, where $\alpha[hkl]$ is the lattice parameter along $[hkl]$ and i, j are integers:

$$\gamma_{\text{effective}}\left(\xi,\zeta\right) = \min_{\substack{\xi = y_1 + y_2 + i\alpha_{[112]} \\ \zeta = z_1 + z_2 + j\alpha_{[110]}}} \Delta\{E\left(y_1, y_2, z_1, z_2\right)\} \tag{2}$$

In this new approach, the relative displacement (ξ, ζ) of one half-crystal with respect to the other half-crystal is performed in two adjacent $\{111\}$ crystallographic planes, see Figure 1. In contrast to [8] and Eq.(1), the obtained "γ-surface" is a function of four coordinates (y_1, y_2, z_1, z_2) and, in its raw form, is of little use

in PFMD. To make it suitable for PFMD modelling, it must be converted to the effective γ-surface as is shown in Equation (2). This implies that among all possible displacements, $\xi = y_1 + y_2 - i\alpha_{[112]}$ and $\zeta = z_1 + z_2 - j\alpha_{[110]}$, the configuration that corresponds to the lowest total energy of the deformed crystal must be taken. The lattice parameters along [112] and [110] are added in order to retain the correct periodic structure of the obtained effective γ-surface.

With this definition, the Mishin EAM potential for the Ni-Al system [10] was employed to calculate both conventional and effective γ-surfaces for both pure nickel and the Ni_3Al intermetallic.

The main difference between the two types of γ-surface is that the high energy faults, that correspond to the highest maxima on the single-layer surface, have been replaced with low-energy minima associated with extrinsic stacking faults. This implies that high energy $ABCCAB$ type stacking is avoided in favour of the $ABCBAB$ type stacking, which bears a much lower energy penalty.

In the case of pure nickel, the high energy fault is replaced by an extrinsic stacking fault ESF. Ni_3Al has two types of these high energy faults, which differ in terms of their their local chemistry. The fault with the higher energy is substituted by the SESF, whereas the one with the lower energy is replaced by a complex extrinsic stacking fault, CESF-1. The structure of this fault is CISF over SISF - it has the same stacking sequence as the SESF (that can be treated as SISF over SISF), but has undesirable local chemistry on one side.

The presence of new minima on the effective γ-surfaces makes available new dislocation dissociation pathways. In the following sections, we show and explain how these changes manifest themselves on the γ' precipitate shearing mechanisms predicted by the phase field model.

3. Model Formulation and Procedure

The phase field model used in this study is largely the same as that used in reference [1] and the common formulation can be found in [2, 4, 5]. The elastic and and gradient free energy, (F_{elastic} and F_{gradient} respectively), as well as the external work, W, terms remained unchanged. The main difference from previous works is the use of new γ-surfaces, which are incorporated into F_{crystal}. But for the large part, this discussion will focus on the results of simulations using the effective γ-surfaces.

In order to adopt the effective γ-surfaces obtained in [7] for use in PFMD we applied the approach of Schoeck [6, 11], where the fitting function is a specially constructed and truncated Fourier series that incorporates the symmetry and periodicity of the crystal. Equation (3) shows the general form of the series, where $\mathbf{g}_k$ are the reciprocal lattice vectors in the co-ordinate system with orthogonal axes (y, z) that run along the $\langle 112 \rangle$ and $\langle 1\bar{1}0 \rangle$ principal crystallographic directions. The number, k, of Fourier coefficients, c_n, depends on the number of known fault energy values, to which the series are fitted.

$$\gamma\left(y,z\right) = \sum_{n=-k}^{k} c_n \exp\left(2\pi i \ \mathbf{g}_n \cdot \mathbf{r}\right) \tag{3}$$

Equation (4) shows the general form of the fitting γ-surface function for the (111) plane used in the present phase field model. This particular form can be used to fit the old single-layer as well as the new effective γ-surfaces in both the γ and γ' phases. Although it appears rather long, with 16 contributing terms, not all of

them are used, depending on the type of the γ-surface and material phase.

$$
\begin{aligned}
\gamma(y,z)=c_0&+c_1[\cos(py)+\cos(0.5py+0.5qz)+\cos(0.5py-0.5qz)]\\
&+c_2[\cos(qz)+\cos(1.5py+0.5qz)+\cos(1.5py-0.5qz)]\\
&+c_3[\cos(2py)+\cos(py+qz)+\cos(py-qz)]\\
&+c_4[\cos(2.5py+0.5qz)+\cos(2py+qz)\\
&+\cos(0.5py+1.5qz)+\cos(0.5py-1.5qz)\\
&+\cos(2py-qz)+\cos(2.5py-0.5qz)]\\
&+c_5[\cos(3py)+\cos(1.5py+1.5qz)+\cos(1.5py-1.5qz)]\\
&+c_6[\cos(2qz)+\cos(3py+qz)+\cos(3py-qz)]\\
&+c_7[\cos(4py)+\cos(2py+2qz)+\cos(2py-2qz)]\\
&+c_8[\cos(3qz)+\cos(4.5py+1.5qz)+\cos(4.5py-1.5qz)]\\
&+c_9[\cos(5py)+\cos(2.5py+2.5qz)+\cos(2.5py-2.5qz)]\\
&+c_{10}[\sin(py)-\sin(0.5py+0.5qz)-\sin(0.5py-0.5qz)]\\
&+c_{11}[\sin(2py)-\sin(py+qz)-\sin(py-qz)]\\
&+c_{12}[\sin(2.5py+0.5qz)-\sin(2py+qz)\\
&-\sin(0.5py+1.5qz)-\sin(0.5py-1.5qz)\\
&+\sin(2py-qz)+\sin(2.5py-0.5qz)]\\
&+c_{13}[\sin(3py)-\sin(1.5py+1.5qz)-\sin(1.5py-1.5qz)]\\
&+c_{14}[\sin(4py)-\sin(2py+2qz)-\sin(2py-2qz)]\\
&+c_{15}[\sin(5py)-\sin(2.5py+2.5qz)-\sin(2.5py-2.5qz)]
\end{aligned}
\tag{4}
$$

The coordinates, y and z, describe displacement along $[\bar{1}2\bar{1}]$ and $[10\bar{1}]$ crystallographic directions respectively. The two lattice periodicity constants are $p{=}2\pi/(\sqrt{3}b)$ and $q{=}2\pi/b$, where $b{=}a/\sqrt{2}$ and a is the lattice parameter. The number of terms in the series depends on the number of fitting points. When constructing the function, it is therefore necessary to identify which points are important in determining the topography of the γ-surface. These are usually, but not exclusively, local minima, maxima and saddle points. Each term must also incorporate the correct rotational symmetry about the origin, which is why it typically consists of at least three sines or cosines in the case of the (111) plane in FCC and $L1_2$. Mirror symmetry must also be taken into account. Along the $[10\bar{1}]$ direction in the (111) plane, the fault energy, γ, follows a profile that shows reflectional symmetry about the y axis. Thus, points lying along this direction are represented by cosines only. There is no such reflectional symmetry along the $[\bar{1}2\bar{1}]$ direction in the (111) plane. Therefore, sine and cosine terms are used in alternation as points that lie along this direction are added.

To define the specific shape of the γ surface, the Fourier coefficients, c_n, must be determined. This is done by solving the linear equation set (5). The vector, $\mathbf{c}$, contains the n unknown coefficients, c_0-c_n. The vector, γ, contains n known values of the GSF energy gamma at chosen knot points, (Y, Z), on the γ-surface. The $n \times n$ matrix $\mathbf{A}$ is constructed from the terms that are multiplied by the Fourier coefficients in Equation (4). Their values can be calculated at each point, (Y, Z),

to complete each row of the matrix.

$$\boldsymbol{\gamma} = \mathbf{A}\mathbf{c} \tag{5}$$

The *Mathematica*® sotware package was used to solve the equation set (5) and obtain the Fourier coefficients. The results are listed in Table 1. It should be noted, that both the construction of the γ-surface function and the selection of knot points are very important. Obtaining a solution to Equation (5) does not guarantee that the γ-surface function will replicate closely, if at all, the shape of the atomistically obtained γ-surface. Likewise, selecting the wrong fitting points will not give an accurate fit even if the constructed function is suitable. The complete list of knot points used and the corresponding fault energy values is given in Table 2. Table 3 lists the fault energies given by each of the functions.

Figure 2 shows the profiles of γ-surfaces along the $\langle 112 \rangle$ and $\langle 110 \rangle$ directions for both Ni and Ni_3Al. The functions are able to reproduce the overall symmetry of the EAM γ-surface, although energy values and co-ordinates of some local minima deviate by as much as 10%. For Ni_3Al, Function B was used over Function C in most phase field simulations, because it followed the atomistic data more closely. It should be noted however, that Function C proved much less sensitive to modification of the fault energies when fitting the coefficients, c_n. In contrast, Function B loses the desired topography faster when attempts at modification are made.

Figure 2 shows well the principal differences between the single-layer and effective γ-surfaces for the two phases. In pure Ni, the high energy A/A stacking fault is resolved by ESF formation. Similarly, in Ni_3Al, the high energy faults A/A and A/A' are resolved by the formation of two-layer CESF-1 and SESF respectively (see Reference [1]). This illustrates that in a crystal system where slip on two planes is allowed, a lower stress is required to deform the material and more dislocation glide patterns are possible.

Figure 3 shows the contour plots of the effective γ-surface functions for the two phases, (Function E for Ni and Function B for Ni_3Al). This graphical representation provides insight into how the dislocations may react or dissociate into partials and also which planar faults will be created as a result. To achieve the lowest energy configuration the dislocations preferentially dissociate so that their constituent Burgers vectors pass through the local minima of the γ-surface and over the saddle points between them. There may be some deviation from the absolute minimum energy path (MEP) on the γ-surface caused by the elastic energy component of PFMD. There is competition between the minimisation of the core energy and minimisation of overall elastic energy. Thus, at higher stresses it is possible for a perfect or superlattice dislocation to dissociate into partials with shorter Burgers vector lengths, but forming a stacking fault with a higher energy than than the minimum possible in the absence of stress. Essentially, the Burgers vectors are being shortened at the expense of higher energy due to a less favourable displacement of the atom layers. The overall Burgers vector of the perfect/superlattice dislocation remains unchanged.

In the phase field model, the total Burgers vector $\mathbf{b}$ is determined by three field variables η_1, η_2 and η_3. These describe the respective contributions of the principal Burgers vectors on the (111) plane: $\mathbf{b}_1 = \frac{a}{2}[0\bar{1}1]$, $\mathbf{b}_2 = \frac{a}{2}[10\bar{1}]$ and $\mathbf{b}_3 = \frac{a}{2}[\bar{1}10]$.

$$\mathbf{b} = \eta_1\mathbf{b}_1 + \eta_2\mathbf{b}_2 + \eta_3\mathbf{b}_3 \tag{6}$$

To complete integration with the PFMD, the gamma surface Equation (4) must be expressed in terms of the field variables by substituting the following into $\gamma(y, z)$

to give $\gamma(\eta_1, \eta_2, \eta_3)$:

$$y = (-\eta_1 + \eta_3)\sqrt{3}b/2 \tag{7a}$$

$$z = (-\eta_1 + 2\eta_2 - \eta_3)b/2 \tag{7b}$$

This allows the γ-surface to be input directly into the crystal free energy term, F_{crystal}, in the phase field model:

$$F_{\text{crystal}} = \int \frac{\gamma(\eta_1, \eta_2, \eta_3)}{d} d\mathbf{r} \tag{8}$$

where d is the slip plane spacing (*i.e.* $d_{(111)}$ in this case).

Since the variables η_1, η_2 and η_3 are non-conserved order parameters, the temporal evolution of the system is given by the time-dependent Ginzburg-Landau equation [12, 13]:

$$\frac{\partial \eta(\mathbf{r}, t)}{\partial t} = -M \frac{\delta F_{\text{total}}}{\delta \eta(\mathbf{r}, t)} \tag{9}$$

$$F_{\text{total}} = F_{\text{elastic}} + F_{\text{gradient}} + F_{\text{crystal}} - W \tag{10}$$

To aid the speed of computation, all known physical quantities were converted to dimensionless reduced units by normalising them according to the grid size of the simulations and the shear modulus of the crystal.

For all the simulations, the mobility constant was selected to be unity (M=1). This is a kinetic coefficient and is proportional to the dislocation mobility, typically with SI units of $\text{m}^2\text{N}^{-1}\text{s}^{-1}$. To determine exact rates observed in the simulations, the temperature dependent values of M would need to be determined experimentally, which is not a simple task and beyond the scope of this work. Since this study focuses on the mechanisms of γ' precipitate shear rather than exact rates of deformation, M was left a dimensionless parameter for the simulations.

Elastic homogeneity was assumed throughout the material. Both phases had the same elastic properties with c_{11}=224, c_{12}=148 and c_{44}=125 GPa . These are experimentally obtained values for Ni_3Al by Kayser and Stassis [14]. The elastic constants and the applied stress were normalised by c_{44} to give the dimensionless quantities for the simulations. Furthermore, the elastic constants were reduced by a factor of 10. Because the elasticity formulation of the model implies a linear scaling dependence of stress on length scale, this had the effect of scaling up the length scale 10 fold. Of course, as the number of grid points in the simulation remains unchanged, the resolution is, in effect, reduced. It should be noted that the assumption of elastic homogeneity in the model implies that there is no load partitioning between the matrix and precipitate phases in the model. In reality, this is not the case in superalloys at primary creep temperatures [15–17]. The difference in elastic moduli between the two phases means that they experience different levels of stress when a load is applied.

Misfit stresses were not incorporated into the model and a sharp interface was assumed between the γ and γ' phases. This way, the γ-surface function changed abruptly from Ni to Ni_3Al when dislocations crossed the interface. The lattice parameter was assumed to be 0.358 nm in both phases, when calculating d in F_{crystal}. Given that the definition of the transformation strain in PFMD [2] and the elastic scaling factor of 10, the grid size equal of the simulation was equal to $d_{\{111\}} \times$

10=2.067 nm. The simulations carried out used periodic boundary conditions and a system size of 660×180×32. One should bear in mind, however, that omitting lattice misfit from the model means that the effects of coherency hardening [18, 19] are taken to be negligible. In comparison, most modern superalloys exhibit a significant negative lattice misfit, *i.e.* the matrix has a larger lattice parameter. The resultant strain field arising at the γ/γ' interface inhibits the entry of dislocations into the precipitates and hence increases the CRSS of the alloys. Nonetheless, since the goal of this work does not encompass making precise CRSS predictions, the absence of lattice misfit and modulus mismatch between γ and γ' phases is an acceptable assumption for the benefit of a model simplicity and reduced computational time.

4. Results and Discussion

The 'Thompson tetrahedron' notation has been used to describe the dislocation configurations observed in the simulations. All simulations were done on the (111) plane, which in this notation system corresponds to the ABC plane, (see Figure 4).

4.1. *Cutting of γ' phase by $a\langle 112\rangle$ ribbons.*

Pure edge, pure screw and mixed character (60° screw) dislocation ribbons were studied over a range of applied stresses (500-1750 MPa). Two types of stress state were considered. In the first case, the stress was applied parallel to the Burgers vector of the whole $a\langle 112\rangle$ ribbon. This way, all four of the comprising $\frac{a}{2}\langle 110\rangle$ dislocations experienced equal resolved stress. In the second case, the stress was applied parallel to one of the two $\frac{a}{2}\langle 110\rangle$ Burgers vectors. Thus, the dislocations with the other $\frac{a}{2}\langle 110\rangle$ Burgers vector experienced only half the resolved stress of the first. This stress bias was introduced to investigate possible changes in shearing mechanisms, similar to the one reported in the previous study [1].

The older model that used only single-layer γ-surfaces, (see Table 1), was also used to study the same dislocation configurations. A comparison of the shearing schemes obtained using the different γ-surface combinations is shown for pure edge dislocations at 1500 MPa in Figure 11.

Let us first consider the case where formation of extrinsic stacking faults is allowed only in the Ni_3Al phase. This was achieved by using the effective γ-surface in the γ' phase only. A single layer γ-surface was used for the γ phase. It was found that for the stress-biased case, the shearing configuration was near identical to that when both phases used single layer γ-surfaces irregardless of dislocation character, (see Figures 11(b) and (c)).

The dislocation ribbon was introduced into the matrix as two $3A\delta$ perfect dislocations. Each of these rapidly dissociated into a AB and AC dislocations. These new perfect dislocations dissociated further into Shockley partial pairs separated by an ISF. This sequence of dissociations is illustrated in Figure 13(a).

$$\begin{aligned} 2\times 3A\delta &\rightarrow 2\times[AB+AC]\rightarrow \\ &\rightarrow 2\times[(\delta B+\mathbf{ISF}+A\delta)+\mathbf{PC}+(\delta C+\mathbf{ISF}+A\delta)] \end{aligned} \tag{11}$$

Upon cutting into the γ' phase, the leading AB dislocation creates an APB in its wake, while a CISF is formed between its constituent partials. The AC dislocation that follows also creates an APB, but the dislocation itself becomes widely extended because a low energy SISF is formed between its partials. The

second AB dislocation also creates an APB, while the last AC returns the crystal to a perfect structure. Both dislocations have a CISF between their partials. The overall configuration is shown by the dashed arrows in Figure 13(c).

$$\begin{aligned} &2\times[(\delta B+\mathbf{ISF}+A\delta)+\mathbf{PC}+(\delta C+\mathbf{ISF}+A\delta)]\rightarrow\\ &\rightarrow(\delta B+\mathbf{CISF}+A\delta)+\mathbf{APB}+(\delta C+\mathbf{SISF}+A\delta)+\mathbf{APB}+\\ &\quad+(\delta B+\mathbf{CISF}+A\delta)+\mathbf{APB}+(\delta C+\mathbf{CISF}+A\delta) \end{aligned} \tag{12}$$

It should be noted, that the transition from stacking fault shear to shearing by APB pairs was not observed as the applied stress was increased. This is contrary to what was observed in the earlier study [1], (see Figure 11(a)). This can be attributed to the use of a different single-layer γ-surface for Ni_3Al. Both γ-surfaces have identical symmetry and feature the same types of planar faults. The coordinates of the local maxima and minima are also near identical. However, the energies associated with the faults differ from those used previously. The most notable differences include the fact that the SISF energy was lowered in [1] from 79 to 12 $\mathrm{mJ\,m^{-2}}$ to fit more closely estimates of the fault energies in Ni-based superalloys. In this study, the single layer γ-surface for Ni_3Al has an SISF energy of 50 $\mathrm{mJ\,m^{-2}}$ as calculated by the Mishin EAM potential [10] . In addition, this EAM potential predicts the CISF energy to be lower than the APB energy. The energy barriers associated with the A/A and A/A' high energy faults were also substantially greater in [1]. Thus, we see that both the magnitudes of the fault energies and the difference between them play an important part in determining the observed shear mechanism. This highlights the importance of considering the topography of the γ-surface as a whole over the individual fault energies when modelling plastic deformation.

In the absence of a stress bias, the shearing of the precipitate starts in the same manner. The mechanism changes during the shearing process in favour of forming an SESF. Figure 5 explains how this mechanism change occurs.

Figure 5(a) and Figure 13(c) show that the initial fault configuration during γ' shearing is the same as in the case of the mixed ribbon.

$$\begin{aligned} &(\delta B+\mathbf{CISF}+A\delta)+\mathbf{APB}+(\delta C+\mathbf{SISF}+A\delta)+\\ &+\mathbf{APB}+(\delta B+\mathbf{CISF}+A\delta)+\mathbf{APB}+(\delta C+\mathbf{CISF}+A\delta)\rightarrow\dots \end{aligned} \tag{13}$$

But in Figure 5(b) and Figure 13(d), it can be seen that the leading partial of the second AC dislocation catches up with the trailing partial of the second AB dislocation. The two partials, $A\delta$ and δC, combine to form an AC dislocation destroying the APB that previously spanned between them.

$$\begin{aligned} &\dots\rightarrow(\delta B+\mathbf{CISF}+AC+\mathbf{SISF}+A\delta)+\\ &+\mathbf{APB}+(\delta B+\mathbf{CISF}+AC+\mathbf{CISF}+A\delta)\rightarrow\dots \end{aligned} \tag{14}$$

This dislocation rapidly dissociates into a leading δC and trailing $A\delta$ partials. Thus, the $A\delta$ and δC Shockley partials effectively cross over to swap places in the overall cutting order. The very low energy of the SESF created, forces the δC to catch up and combine with the δB partial in front of it. This destroys the high energy CISF between them, leaving behind a new $A\delta$ partial dislocation. This final

configuration can be seen in Figure 5(c) and Figure 13(e).

$$\begin{aligned} \ldots \rightarrow (\delta B + \mathbf{CISF} + AC + \mathbf{SISF} + A\delta) + \mathbf{APB} + \\ + (A\delta + \mathbf{SESF} + A\delta + \mathbf{CISF} + A\delta) \end{aligned} \tag{15}$$

While the dislocation-fault sequence changes within the γ' phase, it remains largely unaltered in the γ. This is achieved through the creation of dislocation nodes at or near the matrix-precipitate interface. The detailed structure of the dislocations involved is illustrated in Figure 7.

Now let us consider the case where extrinsic fault formation is allowed in both phases, *i.e.* both the γ and γ' use the effective γ-surface. Irrespective of dislocation character and the magnitude of the applied stress, the observed fault sequence is the same. The presence of a stress-bias, also did not affect this sequence. Thus, only the the pure edge ribbon is considered in the following discussion.

The ribbon, introduced in the matrix phase as two $3A\delta$ perfect dislocations, retains this configuration in contrast to the previous example. Rather than dissociating into a pair of dissimilar $\frac{a}{2}\langle 110\rangle$ type dislocations, each $3A\delta$ dissociates into three identical $A\delta$ Shockley partials. Between these three partial dislocations are two stacking faults: a leading extrinsic fault (ESF) and trailing intrinsic fault (ISF). This way the $\frac{a}{2}\langle 112\rangle$ dislocations are able to stay stable in the γ phase. The corresponding dissociation scheme is illustrated in Figure 13(b).

$$2 \times 3A\delta \rightarrow 2 \times [A\delta + \mathbf{ESF} + A\delta + \mathbf{ISF} + A\delta] \tag{16}$$

Due to this alternative initial configuration in the matrix, the precipitate shearing mechanism is also different, as Figure 6 illustrates. Figure 6(a) shows the first $3A\delta$ dislocation cutting into the precipitate to create an APB. Its overall structure remains the same, but crystal chemistry starts to take effect when creation of stacking faults is concerned. The ESF in γ becomes CESF-1 in the γ', while the ISF becomes SISF. The second $3A\delta$ dislocation enters the γ' to remove the APB and return the crystal to a perfect state. An SESF is formed between its first and second $A\delta$ partials, and a CISF is formed between the second and third (see Figure 6(b)). It can be seen from Figure 6(c), that the dislocation ribbon proceeds in this configuration throughout the entire precipitate until it exits. The overall dissociated configuration of the $6A\delta$ ribbon is shown in Figure 13(f).

$$\begin{aligned} & 2 \times [A\delta + \mathbf{ESF} + A\delta + \mathbf{ISF} + A\delta] \rightarrow \\ & (A\delta + \mathbf{CESF\text{-}1} + A\delta + \mathbf{SISF} + A\delta) + \mathbf{APB} + \\ & + (A\delta + \mathbf{SESF} + A\delta + \mathbf{CISF} + A\delta) \end{aligned} \tag{17}$$

Figure 2 shows that the effective γ-surfaces present a lower energy configuration than their single-layer counterparts. Consequently, the phase field simulations also indicate that formation of extrinsic stacking faults provides the 'path of least resistance' when shearing of the superalloy microstructure is concerned. Indeed, shearing of the whole precipitate is completed significantly more quickly by an edge dislocation when the effective γ-surface is used in both phases (17,200 vs. 25,600 iterations). It allows for an $a\langle 112\rangle$ ribbon configuration that features a smaller number of constituent partial dislocations. Thus, the total number and area of planar faults is also reduced, especially for those that feature local crystal chemistry violations (APB, CISF and CESF).

That said, one should be aware of the limitations of the present phase field model.

It only gives the lowest energy state of the system, without necessarily taking into account how that state is achieved. In particular, the formation of the SESF should be considered. The CESF-1 is formed solely by shear displacement on the adjacent plane along the $\langle 112 \rangle$ direction. The SESF cannot be formed in the same way, because displacement along $\langle 112 \rangle$ would create a different kind of extrinsic stacking fault, the CESF-2 that can be treated as CISF over over CISF in two adjacent $\{111\}$ planes. This defect has the same extrinsic fault stacking sequence, $ABCBAB$, but has the wrong crystal chemistry on both sides. The energy density associated with this fault is very high and its formation is energetically unfavourable.

To create an SESF, an additional relative shear displacement of the two adjacent $\{111\}$ planes by a Burgers vector of $\frac{a}{2}\langle 112 \rangle$ is required. Taking into account the already complex dislocation-fault structure of the ribbon, achieving this additional displacement is mechanically very difficult. However, at elevated temperatures, the SESF could be created via a vacancy mediated atomic shuffle at the leading partial. A similar mechanism at the trailing partial would be needed to remove the SESF. The need for this diffusion controlled process to achieve a configuration with a lower elastic and core energy was originally proposed by Kear *et al.* in 1969 [20, 21]. Decades later, Kovarik *et al.* have used the Density Functional Theory to successfully evaluate the plausibility of this mechanism and the associated energy barriers [22, 23]. Since this diffusion based mechanism is almost certainly the rate determining step for SESF formation in the $a\langle 112 \rangle$ ribbon, it is inaccurate to compare the precipitate shearing rates for the current model. The fact remains, however, that there is always a lower energy path available for γ' cutting, provided this fault is able to form. The need for a vacancy mediated shuffle would explain why the trailing $\frac{a}{3}\langle 112 \rangle$ superpartials of the $a\langle 112 \rangle$ ribbons are found to be pinned at the γ/γ' interface in TEM studies [3, 24]. The recent PFMD work of Zhou *et al.* [25] also shows that the ability to shear γ' precipitates and the observed dislocation configurations depend on the kinetics of diffusional reordering.

Despite this, the use of effective γ-surfaces in PFMD has produced results that are consistent with the final $a\langle 112 \rangle$ dissociation scheme put forward by Kear *et al.* [21]. In this scheme, the γ' precipitates are sheared by three identical $\frac{a}{3}\langle 112 \rangle$ dislocations. This requires three dipole displacements, one at each $\frac{a}{3}\langle 112 \rangle$, to create the energetically favourable configuration of the SISF+SESF stacking fault pair. It was suggested that these displacements should occur readily at elevated temperatures and low strain rates through systematic migration of vacancies at the dislocation core. Kear *et al.* backed their theory with experimental observations of the described shearing scheme [26]. More recently, Rae and Reed published their experimental observations of the same mechanism taking place in the superalloy CMSX-4 [3]. Numerous extended $\frac{a}{2}\langle 112 \rangle$ dislocations were found cutting several γ' precipitates at a time. They were able to span across the narrow γ channels without dissociating into pairs of $\frac{a}{2}\langle 110 \rangle$ dislocations, as can be seen in Figure 14.

The updated PFMD agrees with the aforementioned studies on the fact that creation of SISF+SESF pairs gives the lowest overall energy of the $a\langle 112 \rangle$ dislocation ribbon. However, the structure of the $\frac{a}{3}\langle 112 \rangle$ dislocations involved has not been covered in detail. Particularly, the high energy stacking fault (CISF and CESF-1) are not widely discussed. Rae and Reed do not describe the structure of the trailing and leading $\frac{a}{3}\langle 112 \rangle$ dislocations, but suggest that the middle of the three consists of two Shockley partials bounding a tightly constricted APB. Kear *et al.* state that the leading $\frac{a}{3}\langle 112 \rangle$ is immobilised at the γ/γ' interface because the high energy CESF-1 fault would be created. A dipole displacement is required to transform it to SISF. This acts as a barrier to its further propagation through the precipitate. Propagation can only occur through the diffusion-assisted introduction of a dipole

displacement which creates the low energy SISF instead. The SISF is created in the wake of the CESF-1 purely through shear displacement along $\langle 112 \rangle$ [27, 28]. Furthermore, recent experimental work has found that the leading $\frac{a}{3}\langle 112 \rangle$ encloses a constricted CESF-1 that precedes the SISF [29]. Kear *et al.* also state that the partials of the trailing $\frac{a}{3}\langle 112 \rangle$ return the crystal to its perfect state. Although the authors illustrate it in their schematics, they have not explicitly stated that there is a narrow but distinct CISF between them, as this study has shown.

4.2. *Cutting of γ' by a pair of $\frac{a}{3}\langle 112 \rangle$ dislocations with an overall Burgers vector of $a\langle 110 \rangle$.*

Besides shearing by $a\langle 112 \rangle$ ribbons, alternative mechanisms of γ' precipitate cutting have been proposed. For example, an $a\langle 110 \rangle$ superdislocation can shear the precipitates without leaving behind any defects or dislocation 'debris'. Depending on the relation of the crystal orientation and the applied stress direction (Schmid factor), this type of dislocation may become favoured where a single slip system in the gamma is preferred.

Kear *et al.* [20] proposed that, depending on the APB energy, the $a\langle 110 \rangle$ dislocation would undergo one of two main dissociation schemes in Ni_3Al. If the APB energy is not too high, it would dissociate into two identical $\frac{a}{2}\langle 110 \rangle$ dislocations. Each would in turn consist of two Shockley partials bounding a CISF, as is shown in Figure 9(a).

$$\begin{aligned} 2CB \rightarrow & [CB + \mathbf{APB} + CB] \rightarrow \\ & \rightarrow [(\delta B + \mathbf{CISF} + C\delta) + \mathbf{APB} + (\delta B + \mathbf{CISF} + C\delta)] \end{aligned} \tag{18}$$

Should the APB energy prove too high for the described process, it would then dissociate into two $\frac{a}{3}\langle 112 \rangle$ super partials separated by a superlattice stacking fault. In the case of slip only on one plane (*i.e.* no extrinsic faults), the stacking fault would be an SISF. The superpartials would also dissociate into three Schockley partials forming a CISF and an APB. The configuration in Equation (19) as well as some alternative possibilities are shown in Figure 12.

$$\begin{aligned} 2CB \rightarrow & [2C\delta + \mathbf{SISF} + 2\delta B] \rightarrow \\ & \rightarrow [(\delta A + \mathbf{CISF} + C\delta + \mathbf{APB} + \delta B) + \mathbf{SISF} + \\ & + (C\delta + \mathbf{APB} + \delta B + \mathbf{CISF} + A\delta)] \end{aligned} \tag{19}$$

Despite the relatively low energy of the SISF, the above configuration may not be favoured. The larger Burger's vector of the superpartials, inevitably gives a greater elastic energy. Furthermore, the core energy of the dissociated configuration in Equation (19) would only be lower than that in (18) if the SISF energy is very low [6]. Taking this into account, Kear *et al.* [21] proposed another configuration that could possess a lower core energy. The $\frac{a}{3}\langle 112 \rangle$ dislocations could dissociate into two identical Shockley partials on parallel planes, thus creating a CESF-1. The final structure of the superdislocation is illustrated in Figure 9(f).

$$\begin{aligned} 2CB \rightarrow & [2C\delta + \mathbf{SISF} + 2\delta B] \rightarrow \\ & \rightarrow [(C\delta + \mathbf{CESF\text{-}1} + C\delta) + \mathbf{SISF} + (\delta B + \mathbf{CESF\text{-}1} + \delta B)] \end{aligned} \tag{20}$$

Yamaguchi *et al.* [27] have carried out a comparison of the dissociation schemes in

$L1_2$ crystals as a function of APB and CISF energy, using atomistic simulations. The dissociation scheme shown in Equation (20) has been found to prevail over (18) when the APB energy is high. Changing their complex fault energy did not affect the dissociation.

Kear *et al.* [20] also acknowledged that the $a\langle 110\rangle$ could also dissociate in a manner whereby the order of the two $\frac{a}{3}\langle 112\rangle$ superpartials is reversed. This would create an SESF instead. The authors did not give any details regarding the dissociation of the superpartials. Using the effective γ-surface, it can be seen that a pair of identical Shockley partials separated by a CISF would be created, as is shown in Figure 9(c). For this dissociation scheme to take place, there has to be an active mechanism of creating the SESF, as mentioned in the previous section.

$$\begin{aligned} 2CB \rightarrow & [2\delta B + \mathbf{SESF} + 2C\delta] \rightarrow \\ & \rightarrow [(\delta B + \mathbf{CISF} + \delta B) + \mathbf{SESF} + (C\delta + \mathbf{CISF} + C\delta)] \end{aligned} \tag{21}$$

The effective γ-surface was used to investigate the cutting of a γ' precipitate by configurations in Equations (20) and (21) over a range of applied stresses. The $2CB$ overall edge displacement was introduced as one $2C\delta$ and one $2\delta B$ dislocations in the matrix. Both of the two possible arrangements were studied (i.e. leading $2C\delta$ and leading $2\delta B$). In the γ phase, the $2CB$ dislocation was stable in both arrangements, despite the larger Burgers vectors of the constituent dislocations and the additional stacking faults that are created.

$$[2C\delta + \mathbf{ISF} + 2\delta B] \rightarrow [(C\delta + \mathbf{ESF} + C\delta) + \mathbf{ISF} + (\delta B + \mathbf{ESF} + \delta B)] \tag{22}$$

$$[2\delta B + \mathbf{ESF} + 2C\delta] \rightarrow [(\delta B + \mathbf{ISF} + \delta B) + \mathbf{ESF} + (C\delta + \mathbf{ISF} + C\delta)] \tag{23}$$

Owing to these stable starting configurations, the $2CB$ dislocation is able to cut the γ' precipitate as a pair of $\frac{a}{3}\langle 112\rangle$ superpartials via the creation of an SISF or SESF. Figure 8 shows a comparison of the two possible mechanisms. The dislocation structures in the γ' phase are consistent with those described by Kear *et al.* (Refer to Figures 9(f) (SISF) and 9(c) (SESF).)

The SESF and SISF energies are similar in magnitude, while the CESF-1 energy is approximately 31-37% greater than that of the CISF. Thus, the configuration that produces the SESF has a lower core energy. It requires fewer iterations in the PFMD to produce a given amount of γ' deformation, when compared to the alternative combination that creates an SISF. However, as was discussed in the previous section, SESF formation is not instantaneous.

PFMD shows that an $a\langle 110\rangle$ dislocation can be stable as a pair of $\frac{a}{3}\langle 112\rangle$ dislocations in both γ and γ'. Therefore, the stacking faults are able to span continuously across the precipitates and the matrix channels. This eliminates the need for any constrictions at the interface. However, formation of such pairs in the γ phase is unlikely because $\frac{a}{2}\langle 110\rangle$ is the preferred dislocation in FCC materials. The phase field model is consistent with this. When a whole $2CB$ dislocation is introduced in the γ phase, it dissociates into a pair of CB dislocations. If the configuration consisting of superpartials is unable to nucleate in the matrix, it has to do so in the precipitate. The model suggests there is no tendency to do this. This can be rationalised since the mutual elastic repulsion of the two $\frac{a}{2}\langle 110\rangle$ type dislocations would have to be overcome to achieve a lower core energy.

4.3. *Cutting of γ' by a pair of identical $\frac{a}{2}\langle 110\rangle$ dislocations.*

Based on the findings described in the previous subsection, it was decided to use the phase field model to investigate the mechanism of spontaneous nucleation of a superpartial pair from an APB pair during the shearing of the precipitate. APB pairs have been studied extensively, both experimentally and using various numerical models, in single phase $L1_2$ materials, especially Ni_3Al.

A $2CB$ dislocation was introduced into the matrix phase. This ensured minimum separation between the two CB dislocations after dissociation of the original dislocation. $2CB$ dislocations of both screw and edge character were investigated. Each CB dislocation dissociated into a leading $C\delta$ and trailing δB (Figure 9(a)). Applied stress values for the simulations ranged from 500 to 1000 MPa. The stress was applied along the directions CB, $C\delta$ and δB. The latter two aimed to investigate whether a bias in stress on one of the partials would promote a reaction that would nucleate a superpartial pair.

Despite the wide range of conditions that was surveyed, pairs of $\frac{a}{3}\langle 112\rangle$ dislocations were unable to form from the initial configuration. The two CB dislocations proceeded to cut the entire γ' precipitate with a tightly constricted APB between them. This configuration is compact and leaves behind a perfect crystal. In the framework of the model, reconfiguring to a pair of superpartials does not offer a sufficient advantage in terms of energy. The number of Shockley partials would remain unchanged: it is equal to four in both cases. But the elastic energy would increase irrespective of any possible decreases in core energy. Creation of an SESF would require the reordering of the two middle Shockley partials (Figures 9(b),(c)), *i.e.* one dislocation would have to overtake the other and at this point the Burgers Vector would be CB as indicated on Figure 9(b). This is opposed by the energy barrier associated with a large local maximum. Despite the low energy of the SESF compared to APB, the described barrier is too substantial for the overall energy minimisation of the model. Let us consider the scheme involving creation of an SISF (Figures 9(d),(e),(f)). It would first require the reversal of Shockley partial order in each of the CB dislocations (Figure 9(d)). This not only gives very large core energies to both partials, but also creates CESF-1, which is of higher energy than the previous CISF. This initial requirement goes against energy minimisation.

4.4. *Cutting of γ' by a single $\frac{a}{2}\langle 110\rangle$ dislocation.*

Another mechanism for γ' precipitate cutting has been put forward by Decamps *et al.* [30–33]. The authors propose that a single $\frac{a}{2}\langle 110\rangle$ dislocation is able to shear a precipitate. This is made possible, due to a Shockley partial loop that nucleates at the matrix-precipitate interface and destroys the resultant APB to create either an SISF or SESF. Thus, the γ' precipitate is cut by an $\frac{a}{3}\langle 112\rangle$ superpartial, while an $\frac{a}{6}\langle 112\rangle$ Shockley partial is left at the precipitate boundary. At the interface the two dislocations combine at a node to give the original $\frac{a}{2}\langle 110\rangle$ dislocation that continues to shear the matrix.

$$CB + \mathbf{APB} + \bigcirc A\delta \rightarrow 2C\delta + \mathbf{SISF} + A\delta \tag{24}$$

$$CB + \mathbf{APB} + \bigcirc \delta A \rightarrow 2\delta B + \mathbf{SESF} + \delta A \tag{25}$$

The symbol $\bigcirc$ denotes the dislocation loop. In the context of the Decamps *et al.* mechanism, it is equivalent to adding the negative of the denoted Shockley partial before adding that Shockley partial itself. This retains the previous overall $\frac{a}{2}\langle 110\rangle$

type displacement, but gives a different dissociated structure. The fully dissociated structure should be as follows:

$$\begin{aligned}&(\delta B + \mathbf{CISF} + C\delta) + \mathbf{APB} + (\delta A + \mathbf{SISF} + A\delta) \rightarrow \\ &\rightarrow (C\delta + \mathbf{CESF} + \delta B) + \mathbf{APB} + (\delta A + \mathbf{SISF} + A\delta) \rightarrow \\ &\rightarrow C\delta + \mathbf{CESF} + C\delta + \mathbf{SISF} + A\delta\end{aligned} \tag{26}$$

$$\begin{aligned}&(\delta B + \mathbf{CISF} + C\delta) + \mathbf{APB} + (A\delta + \mathbf{SESF} + \delta A) \rightarrow \\ &\rightarrow \delta B + \mathbf{CISF} + \delta B + \mathbf{SESF} + \delta A\end{aligned} \tag{27}$$

Decamps *et al.* suggested that the SISF is created when the trailing partial of the original $\frac{a}{2}\langle 110\rangle$ dislocation experiences a greater resolved stress than the leading one. This is likely when the single crystal alloy is in tension. The difference in resolved stress is to force the dislocations to reverse order in the γ', this would favour the nucleation of a Shockley partial loop that bounds an SISF. When the leading partial has a greater or equal stress compared to the trailing, the original order is maintained and SESF is favoured. This case is expected to be more common in compression.

The precipitate cutting schemes of Decamps *et al.* were not observed in our PFMD simulations, although a wide variety of conditions have been attempted. Calculations were performed for both screw and edge CB dislocations over a range of applied stresses, which were biased towards the leading, trailing or neither of the Shockley partials. At greater values of applied stress the CB dislocation was able to cut the precipitate despite the high energy of the APB. When the stress was insufficient to completely cut the precipitate, the CB dislocation lopped around it in the matrix. In the latter case, the leading Shockley partial was able to penetrate the γ' precipitate to a limited extent and create a CISF. The same set of simulations was repeated with the Ni_3Al γ-surface modified so that the SISF and SESF values were reduced to 20% of their original values. Function C, rather than Function B, was used for the modified effective γ-surface. The former better retains the correct geometry and periodicity when the fault energies are scaled. The additional PFMD simulations still showed that the discussed shearing mechanisms failed to initiate.

The results of the phase field model indicate that the nucleation of a partial loop was not energetically favourable (Figure 10). This is a consequence of the topography of the effective γ-surface. The scheme that creates an SISF requires a reversal of order from the Shockley partials (Figure 10(d)). The CESF has a 31-37% higher energy than the CISF. Furthermore the two partials have to overcome the barriers associated with high energy faults (local maximum on γ-surface). This would give very large core energies to both partials before the proposed loop is nucleated (Figure 10(e))- one that is larger than that of the existing dislocation and goes against the energy minimisation of the phase field model. Similarly, in the scheme that creates an SESF, the last partial would have a very large core energy because the Shockley partials of the nucleated loop overcome a very high local maximum giving prohibitively high core energies (Figures 10(b),(c)). The nucleation of the SESF containing loop is therefore not favoured.

5. Conclusion

The new effective γ-surfaces proposed in [7] give a more accurate representation of the energetics governing the structure and movement of dislocations in two-phase Ni-based superalloys. With these γ-surfaces it has been possible to analyse a wider range of dislocation structures in particular those involving extrinsic stacking faults.

The phase field model uses the energy topography represented by the γ-surface to balance the elastic energy generated by the Burgers vector of the dislocations and their partials and the core energy from the displacement of the crystal planes from their equilibrium positions. In this context, the topography of the γ-surface between the minima is as important as the fault energies themselves represented by the values of the minima. The phase field model also allows for the formation of faults bounded by partial dislocations whose Burgers vectors are not rational fractions of the overall Burgers vector. The effective Burgers vector of the partials can be shortened reducing the elastic energy but increasing the fault energy. This effect is most notable in cases where the γ-surface has a gentle gradient adjacent to the local minimum of the fault. It is also clear from the results presented that the configuration of the dislocation in the gamma phase prior to entry into the precipitate has a profound influence on the dissociations which occur during the transit through the γ' precipitates. Thus, the fault energy in the matrix phase might be expected to have an effect on mechanism just as the fault energies in the precipitate itself. It is also found that the dislocation structures defined at the start of the calculation have a significant effect on the outcome. This raises the question of how well the model copes with processes such as the formation of the $\frac{a}{3}\langle 112\rangle$ dislocations where there is a significant energy barrier to the formation of a lower energy configuration and one which has been shown to be stable if introduced explicitly into the model.

In this study, three cases have been examined: $a\langle 112\rangle$ ribbons; $a\langle 110\rangle$ dislocation pairs and $\frac{a}{2}\langle 110\rangle$ single matrix dislocations.

Dislocation ribbons with an overall Burgers vector of $a\langle 112\rangle$ are widely observed during the early stages of primary creep where the overall dislocation penetration is low. The model has shown that the $\frac{a}{2}\langle 112\rangle$ Burgers vector is stable in the γ phase, as observed in Figure 14, and that on entering the γ', the low energy of the SISF and the SESF cause the wide dissociation of each dislocation to give the stacking fault shear configurations seen. It is notable that where the single layer γ-surface was used in the matrix, a difference between the mixed and edge configurations was seen, with the mixed dislocations adopting a single layer configuration containing only intrinsic faults reproducing that in the γ phase during transit of the γ'precipitate. However, when the applied stress vector is parallel to the total Burgers vector, the $a\langle 112\rangle$ dislocation undergoes a transition to produce the low energy SESF in the trailing part of the ribbon, this necessitates constrictions at the γ/γ' interface as the partials cross over. When the effective γ-surfaces are employed in both phases, the same configuration is seen irrespective of the character of the dislocation or the level of the stress and its bias towards one of the two component $\frac{a}{2}\langle 110\rangle$ vectors. The structures produced by the model differ from those observed in TEM in one particular respect. The dislocations bounding the SESF enter the γ' phase with ease giving a relatively narrow SESF. In comparison, TEM observations show the dislocations to be held at the point of entry into the γ' phase. This is a result of the possible lattice shuffles necessary to produce and eliminate a SESF in the ordered structure, which the model does not include. The transition to individual $\frac{a}{2}\langle 110\rangle$ dislocation pairs at high stress is not seen.

Superlattice dislocations composed from two similar matrix dislocations of overall Burgers vector $a\langle 110\rangle$ were then examined. In the first instance, the dislocation was introduced as two superpartials having either a SESF or a SISF between them. Both proved stable in both phases when introduced as super partials, but it was not possible to stimulate dissociation of the two $\frac{a}{2}\langle 110\rangle$ dislocations to produce the superpartials in the phase field model, despite a range of shear magnitudes and geometries tried. This would require the constriction and crossover of two partials and examination of the γ-surface indicates this would require considerable activation to achieve. The difficulties related to the activation required to form SESF or SISFs correlate well with the observation that stacking fault shear is not seen where there are no dislocations in the matrix whose Burgers vectors combine to give $\frac{a}{2}\langle 112\rangle$ [34]. Hence, we conclude that the direct formation of super partials from $a\langle 110\rangle$ dislocations requires a very considerable activation.

Finally, we investigated a third method of forming superlattice partials proposed by Decamps *et al.* [30–33]. In this mechanism a superlattice partial is produced from a single matrix dislocation by the nucleation of a partial loop at the γ/γ' interface. We were unable to replicate this mechanism in the phase field model despite a wide range of stresses and deformation geometries attempted. This indicated that, for it to occur, considerable thermal nucleation is also likely to be necessary.

6. Acknowledgements

The authors would like thank the following people for their invaluable assistance with theory and discussion: Prof. Gunther Schoeck of Universität Wien, Prof. Yunzhi Wang and Dr. Ning Zhou of the Ohio State University and Prof. Roger Reed of the University of Birmingham. Funding from EPSRC under grant number EP/D047684/1 (Alloys by Design) is also acknowledged with gratitude.

References

[1] V.A. Vorontsov, C. Shen, Y. Wang, D. Dye and C.M.F. Rae, Acta Materialia 58 (2010) p. 4110–4119.
[2] Y.U. Wang, Y.M. Jin, A.M. Cuitiño and A.G. Khachaturyan, Acta Materialia 49 (2001) p. 1847–1857.
[3] C.M.F. Rae and R.C. Reed, Acta Materialia 55 (2007) p. 1067–1081.
[4] C. Shen and Y. Wang, Acta Materialia 51 (2003) p. 2595–2610.
[5] C. Shen and Y. Wang, Acta Materialia 52 (2004) p. 683–691.
[6] G. Schoeck, S. Kohlhammer and M. Fähnle, Philosophical Magazine Letters 79 (1999) p. 849–857.
[7] R.E. Voskoboinikov and C.M.F. Rae, IOP Conference Series: Materials Science and Engineering 3 (2009) p. 012009.
[8] V. Vitek, Philosophical Magazine 18 (1968) p. 773–786.
[9] F.C. Frank, Philosophical Magazine (Series 7) 42 (1951) p. 809–819.
[10] Y. Mishin, Acta Materialia 52 (2004) p. 1451–1467.
[11] G. Schoeck, Materials Science and Engineering A 400-401 (2005) p. 7–17 Dislocations 2004.
[12] V.V. Bulatov and W. Cai, *Computer Simulations of Dislocations*, Oxford University Press, 2006.
[13] L.Q. Chen and Y. Wang, JOM 48 (1996) p. 13–18.
[14] F.X. Kayser and C. Stassis, Physica Status Solidi A 64 (1981) p. 335–342.
[15] D. Dye, J. Coakley, V.A. Vorontsov, H.J. Stone and R.B. Rogge, Scripta Materialia 61 (2009) p. 109–112.
[16] V.A. Vorontsov and H.J. Stone Manuscript in preparation.
[17] D. Siebörger, H. Knake and U. Glatzel, Materials Science and Engineering A 298 (2001) p. 26–33.
[18] V. Gerold and H. Haberkorn, Physica Status Solidi 16 (1966) p. 675–684.
[19] R.F. Decker, *Strengthening mechanisms in nickel-base superalloys*, in *Steel Strengthening Mechanisms (Symposium)* Republished by TMS for Superalloys 2008, 1969, pp. 147–170.
[20] B.H. Kear, A.F. Giamei, G.R. Leverant and J.M. Oblak, Scripta Metallurgica 3 (1969) p. 123–129.
[21] B.H. Kear, A.F. Giamei, G.R. Leverant and J.M. Oblak, Scripta Metallurgica 3 (1969) p. 455–460.
[22] L. Kovarik, R.R. Unocic, J. Li, P. Sarosi, C. Shen, Y. Wang and M.J. Mills, Progress in Materials Science 54 (2009) p. 839–873.
[23] L. Kovarik, R.R. Unocic, J. Li and M.J. Mills, JOM 61 (2009) p. 42–48.
[24] G.R. Leverant and B.H. Kear, Metallurgical Transactions 1 (1970) p. 491–498.
[25] N. Zhou, C. Shen, M.J. Mills, J. Li and Y. Wang, Acta Materialia 59 (2011) p. 3484 – 3497.
[26] B.H. Kear, J.M. Oblak and A.F. Giamei, AIME Transactions 1 (1970) p. 2477–2485.

REFERENCES

[27] M. Yamaguchi, D.P. Pope, V. Paidar and V. Vitek, Philosophical Magazine A 45 (1982) p. 867–882.
[28] R. Voskoboinikov and C. Rae To be published.
[29] V.A. Vorontsov, L. Kovarik, M.J. Mills and C.M.F. Rae Manuscript in preparation.
[30] M. Condat and B. Décamps, Scripta Metallurgica 21 (1987) p. 607–612.
[31] B. Décamps, A.J. Morton and M. Condat, Philosophical Magazine A 64 (1991) p. 641–668.
[32] B. Décamps and A..J. Morton, Philosophical Magazine A 68 (1993) p. 1129–1149.
[33] B. Décamps, S. Rajoul, A. Coujou, F. Pettinari-Sturmel, N. Clément, D. Locq and P. Caron, Philosophical Magazine 84 (2004) p. 91–107.
[34] C.M.F. Rae, N. Matan, D.C. Cox, M.A. Rist and R.C. Reed, Metallurgical and Materials Transactions A 31 (2000) p. 2219–2228.
[35] G. Schoeck, *Private communication*; .
[36] C.L. Fu and M.H. Yoo, in *MRS Symposium Proceedings*, Vol. 133 MRS, 1989, pp. 81–86.
[37] O.N. Mryasov, Y.N. Gornostyrev, M. Schilfgaardevan and A.J. Freeman, Acta Materialia 50 (2002) p. 4545–4554.
[38] N.M. Rosengaard and H.L. Skriver, Physical Review B 50 (1994) p. 4848–4858.
[39] P. Veyssière, J. Doin and P. Beuchamp, Philosophical Magazine A 51 (1985) p. 469–483.
[40] H.P. Karnthaler, E.T. Mühlbacher and C. Rentenberger, Acta Materialia 44 (1996) p. 547–560.
[41] K.J. Hemker and M.J. Mills, Philosophical Magazine A 68 (1993) p. 305–324.

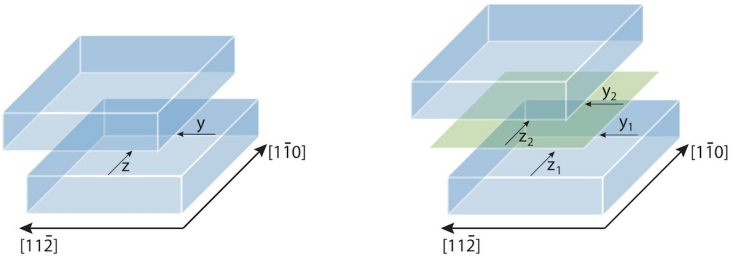

Figure 1. Methodology comparison between calculating a conventional single-layer (a) and the effective (b) γ-surface [7].

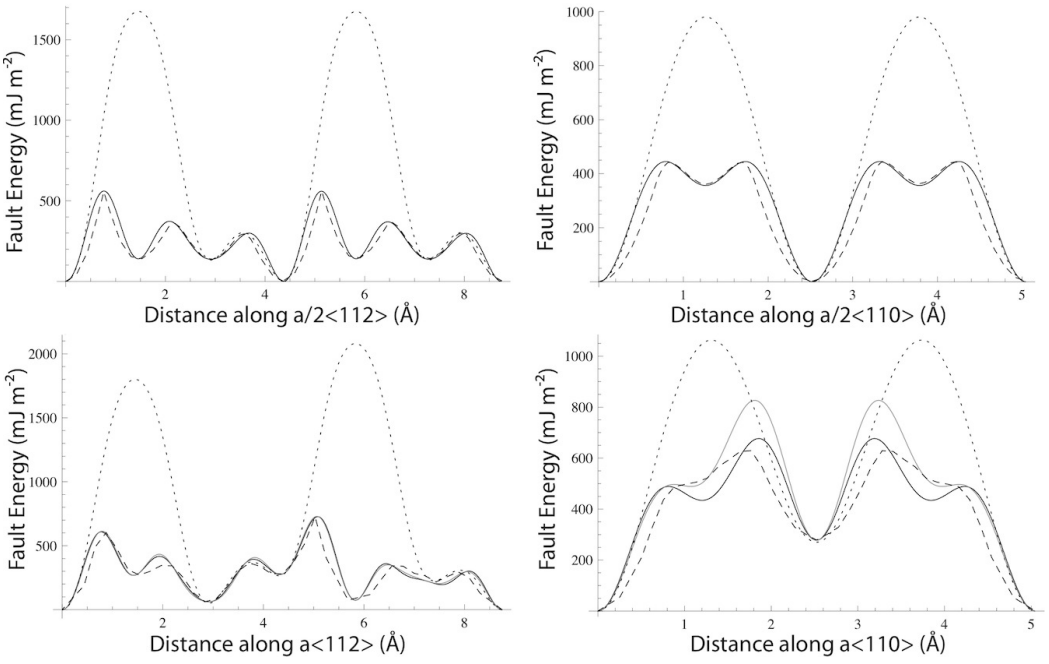

Figure 2. Profile comparison of γ-surfaces along the $\langle 112 \rangle$ and $\langle 110 \rangle$ directions for pure Ni and Ni_3Al. For Ni, the solid line shows the effective γ surface Function E, the dashed line is the corresponding EAM data, while the dotted line is the single-layer Function D. In the case of Ni_3Al, the solid black and grey lines correspond to the effective γ-surface Function B and Function C respectively, the dashed line is EAM data and the dotted line is the single-layer Function A.

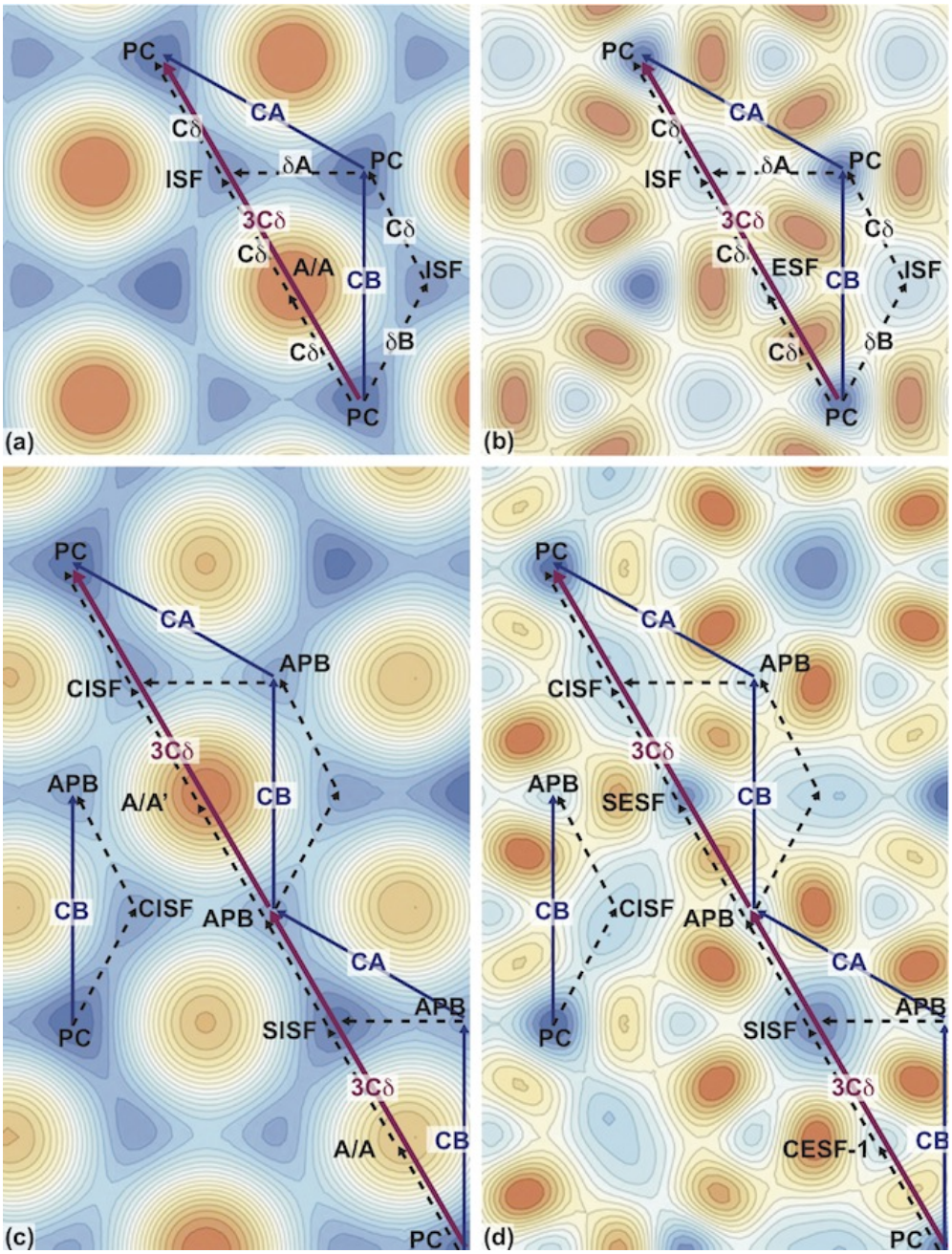

Figure 3. Contour plots of the γ-surface functions used in the phase field model: (a) single-layer γ-surface Function D for pure Ni, (b) effective γ-surface Function E for pure Ni, (c) single-layer γ-surface Function A for Ni_3Al and (d) effective γ-surface Function B for Ni_3Al. Possible dissociation reactions are shown for $\frac{a}{2}\langle 112\rangle$ in Ni and $a\langle 112\rangle$ in Ni_3Al.

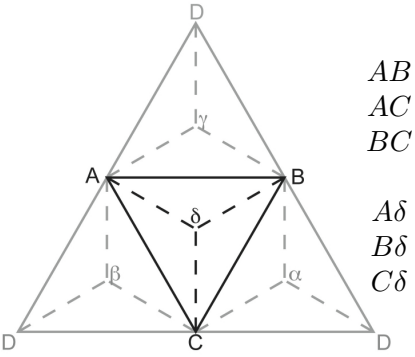

$$AB = \frac{a}{2}[\bar{1}10] \qquad BA = \frac{a}{2}[1\bar{1}0]$$
$$AC = \frac{a}{2}[01\bar{1}] \qquad CA = \frac{a}{2}[0\bar{1}1]$$
$$BC = \frac{a}{2}[10\bar{1}] \qquad CB = \frac{a}{2}[\bar{1}01]$$

$$A\delta = \frac{a}{6}[\bar{1}2\bar{1}] \qquad \delta A = \frac{a}{6}[1\bar{2}1]$$
$$B\delta = \frac{a}{6}[2\bar{1}\bar{1}] \qquad \delta B = \frac{a}{6}[\bar{2}11]$$
$$C\delta = \frac{a}{6}[\bar{1}\bar{1}2] \qquad \delta C = \frac{a}{6}[11\bar{2}]$$

Figure 4. Unfolded net of the Thompson tetrahedron used to describe slip in FCC crystals. Triangles ABC, ACD, BCD and ABD represent slip planes (111), $(1\bar{1}\bar{1})$, $(\bar{1}1\bar{1})$ and $(\bar{1}\bar{1}1)$ respectively.

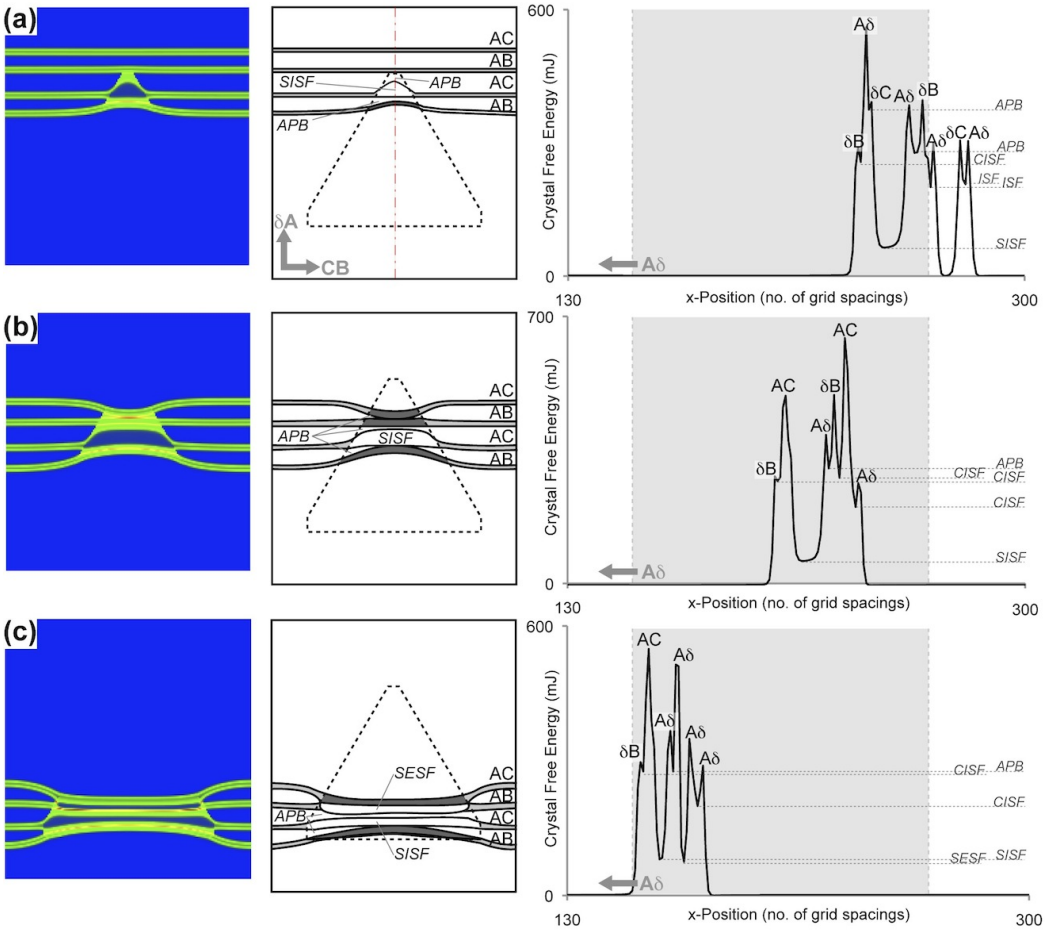

Figure 5. Analysis of results obtained with a 750 MPa stress applied along $A\delta$ using an effective γ-surface in the precipitate phase only. Rearrangement of the partial dislocations nucleates a low energy SESF. Evolution stages at t =560, 1200 and 2200 are shown, with Δt=0.1.

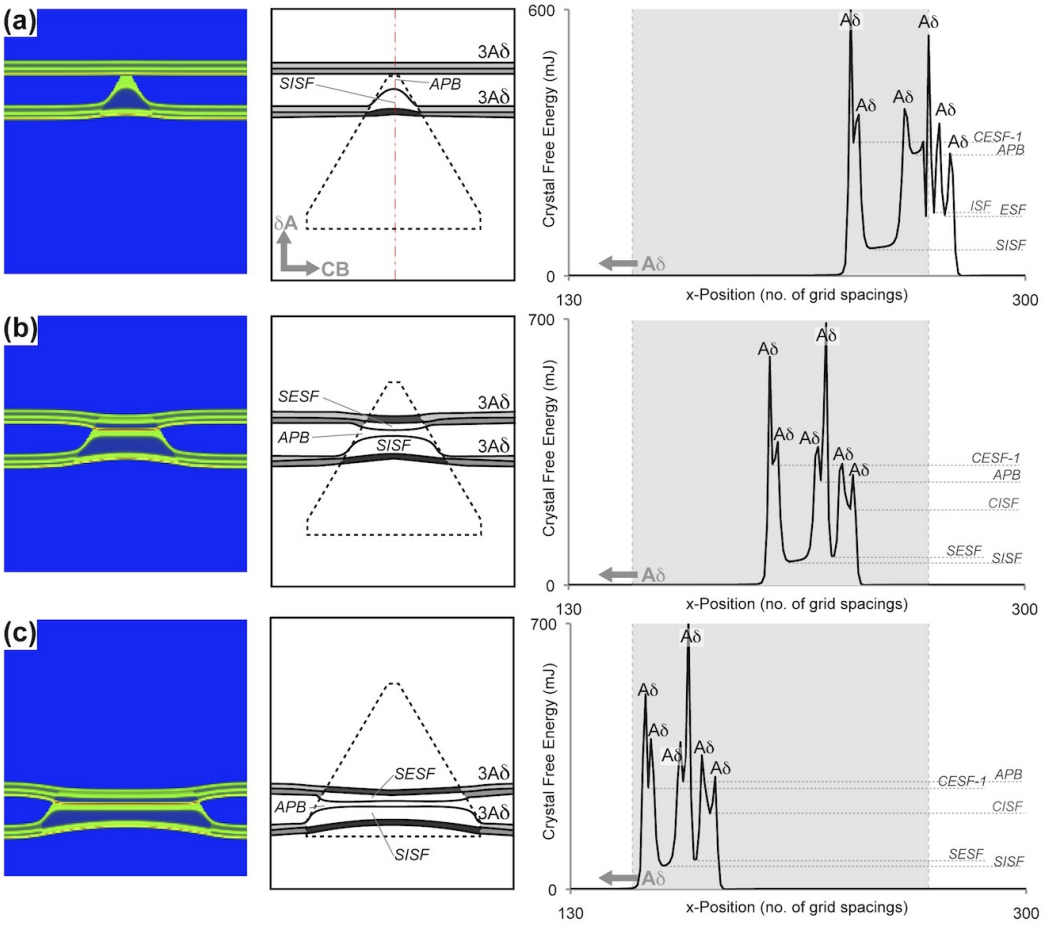

Figure 6. Analysis of results obtained with a 750 MPa stress applied along $A\delta$ using an effective γ-surface in both matrix and precipitate. The initial configuration in the matrix gives rise directly to an SISF-SESF pair in the precipitate. Evolution stages at t =520, 1040 and 1840 are shown, with Δt=0.1.

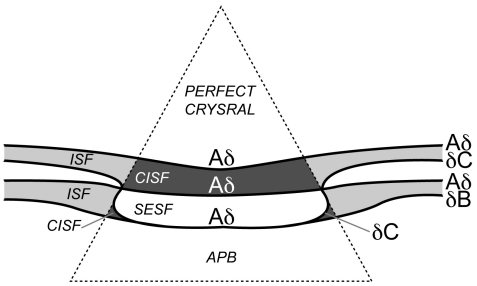

Figure 7. Detailed schematic representation of the dislocation-fault configuration illustrated in Figure 5(c).

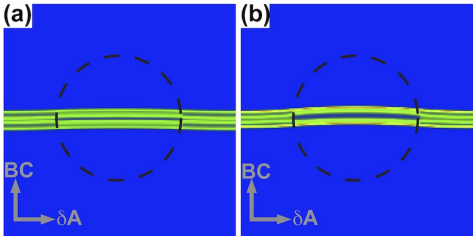

Figure 8. Cutting of a round γ' precipitate by a pair of $\frac{a}{3}\langle 112\rangle$ superpartials bounding an SESF (a) and SISF (b) at 750 MPa applied along CB. The number of iterations is 11500 and 13500 for cases (a) and (b) respectively.

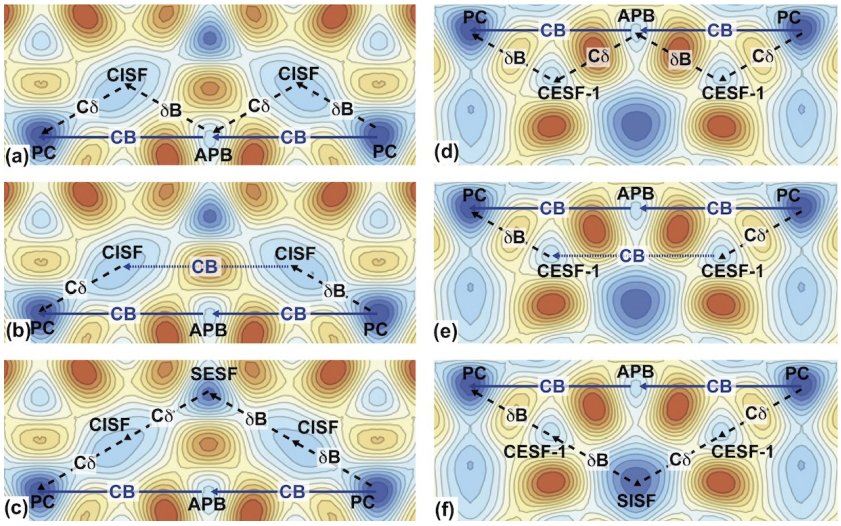

Figure 9. Original form of the $2CB$ dislocation is shown in (a). To transform it to superpartials bounding an SESF, steps in (b) and (c) are required. To obtain superpartials bounding and SISF, steps (d), (e) and (f) must be completed.

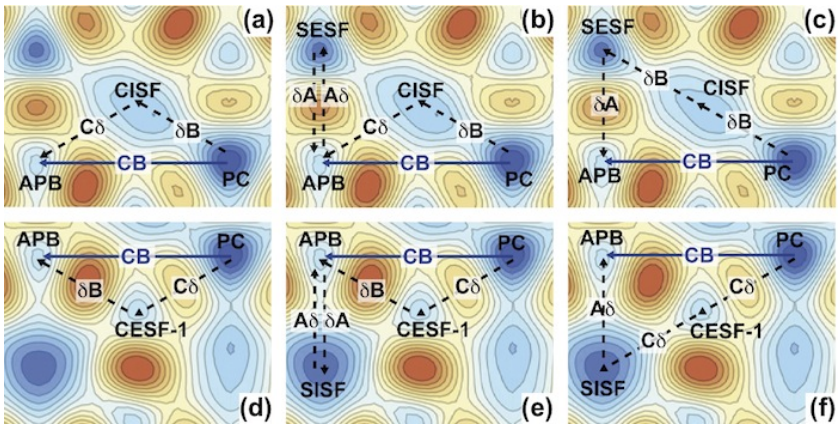

Figure 10. Original CB dislocation is given in (a). Steps (b) and (c) show how a Shockley partial loop bounding an SESF could change the overall configuration. Steps (d), (e) and (f) show the creation SISF bounding loop and the resultant configuration. PFMD simulations have shown that these transformations, proposed by Decamps *et al.*, are not energetically favourable.

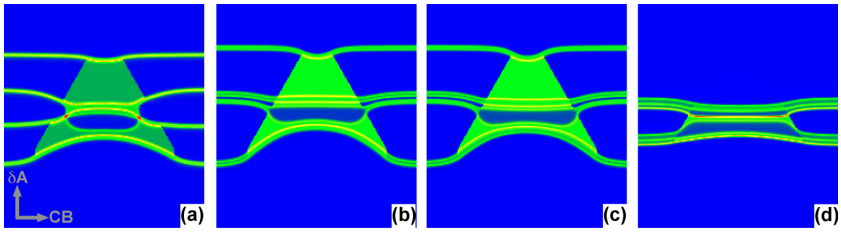

Figure 11. Cutting of the γ' precipitate by an $A\delta$ edge dislocation using four different γ-surfaces at an applied stress of 1500 MPa applied along AB: (a) single-layer γ-surface in both phases as used in [1], (b) single-layer γ-surface in both phases, (c) effective γ-surface in γ' only, (d) effective γ-surface in both phases. All pictures show state of the system after 9,000 iterations.

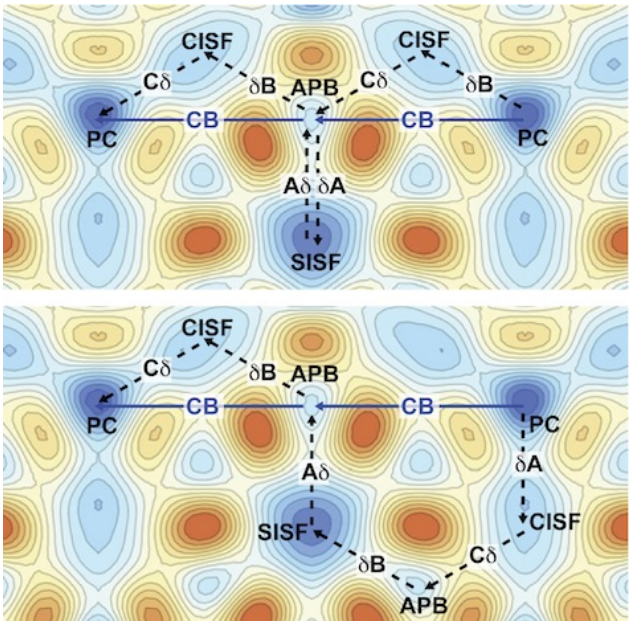

Figure 12. Possible dissociation schemes for a $2CB$ superdislocation that would be required to produce the configuration featuring an SISF if extrinsic stacking faults are not allowed to form. The scheme in Equation (19) is illustrated in the bottom image.

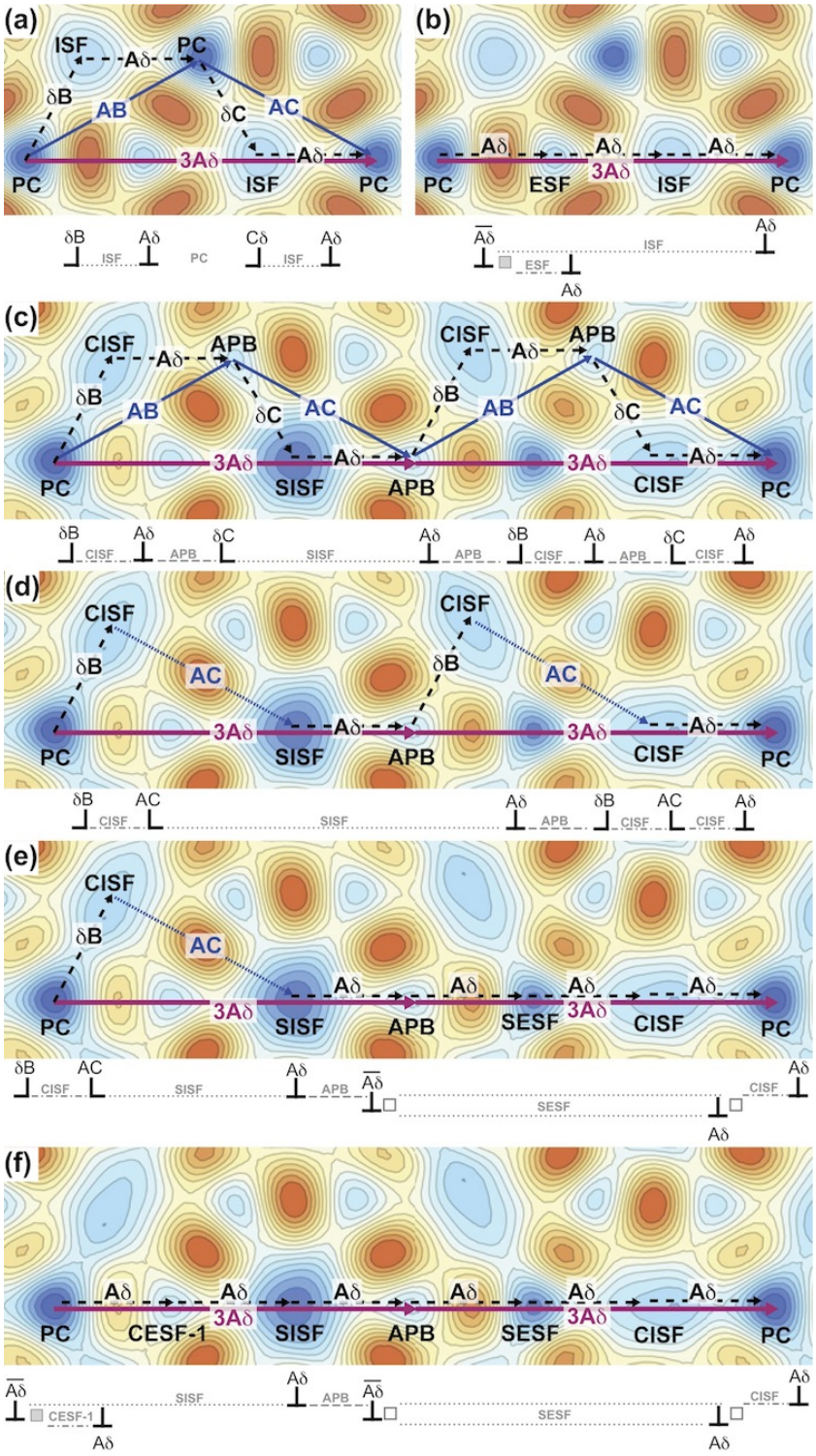

Figure 13. Dissociation sequences of $\frac{a}{2}\langle 112\rangle$ dislocations in the γ and $a\langle 112\rangle$ ribbons in the γ' observed in the PFMD simulations as illustrated in Figures 5 and 6. The notation of Kear *et al.* [20, 21, 26] has been added under each γ-surface diagram. The bar over the dislocation symbol indicates that the dislocation creates an extrinsic stacking fault and its line effectively lies between the two adjacent slip planes. The squares represent an $\frac{a}{2}\langle 110\rangle$ dipole displacement at or near the core of the preceding dislocation. The unshaded squares represent the requirement of a vacancy mediated shuffle to create the SESF. Where the squares are shaded grey, the corresponding extrinsic fault structure is created purely by shear displacements.

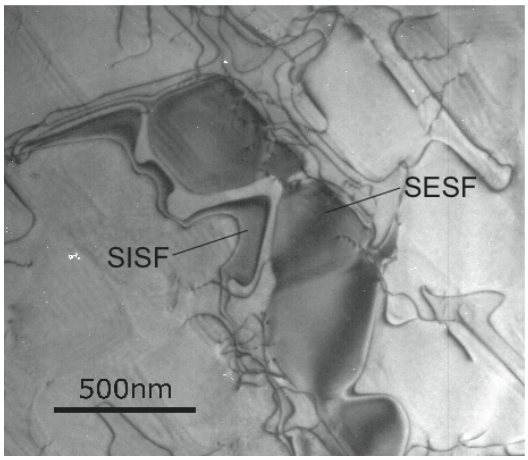

Figure 14. TEM micrograph showing an example of an $a\langle 112\rangle$ dislocation ribbon propagation on a {111} plane of a TMS-82+ superalloy single crystal deformed under primary creep conditions (750°C and 750 MPa) to 1.4% strain. The ribbon features widely extended SISF and SESF formed in successive rows of γ' precipitates [1].

Table 1. Fourier coefficients used to define the γ-surfaces in conjunction with Equation (4).

γ-surface	A	B	C	D	E
Phase	Ni_3Al	Ni_3Al	Ni_3Al	Ni	Ni
Layers	1	2	2	1	2
c_0	851.1	433.4	464.6	709.4	325.4
c_1	-52.0	-22.3	-22.3	-212.1	0
c_2	-10.7	-53.0	-79.1	-35.6	0
c_3	-193.6	31.2	31.2	8.5	-11.8
c_4	-0.3	0	0	1.3	0
c_5	-4.3	5.7	26.5	0	-0.9
c_6	-32.0	-76.7	-87.1	0	-77.7
c_7	9.4	-29.4	-29.4	0	-18.9
c_8	0	-5.3	0	0	0.9
c_9	0	5.4	5.4	0	0
c_{10}	70.0	-0.6	-0.6	-320.0	0
c_{11}	-342.4	-55.7	-55.7	-21.5	-37.8
c_{12}	-1.1	0	0	0.8	0
c_{13}	-5.0	4.4	4.4	0	0
c_{14}	-19.6	-47.6	-47.6	0	-37.2
c_{15}	0	5.2	5.2	0	0

Table 2. Coordinates of knot points used for solving Equation (5) points and their corresponding fault energy density values (in $\mathrm{m\,Jm^{-2}}$). The original set of knot points for Ni_3Al was suggested by Schoeck [6, 35] and are indicated with an asterisk symbol (∗). It was necessary to introduce and/or remove knot points in this initial set in order to correctly fit the gamma surfaces used in this work. The fault energy values corresponding to the knot points were taken from single-layer and effective γ-surfaces calculated using EAM employing the inter-atomic potential of Mishin [10]. The methodology for the evaluation of these γ-surfaces in Ni_3Al is described in [7]. This approach was also used for the γ-surfaces in pure nickel, which will be published elsewhere.

γ-surface	A	B	C	D	E
Phase	Ni_3Al	Ni_3Al	Ni_3Al	Ni	Ni
Layers	1	2	2	1	2
$\gamma\,(0,0)*$	0	0	0	0	0
$\gamma\,(h/6,0)*$	1000	603	603	-	556
$\gamma\,(h/3,0)*$	1800	271	271	810	140
$\gamma\,(h/2,0)*$	1000	343	343	1520	360
$\gamma\,(2h/3,0)*$	50	62	62	1670	137
$\gamma\,(-h/6,0)*$	300	296	296	-	298
$\gamma\,(-h/3,0)*$	240	219	219	280	137
$\gamma\,(-h/2,0)*$	1300	344	344	240	360
$\gamma\,(-2h/3,0)*$	2080	74	74	140	140
$\gamma\,(0,b)*$	270	278	278	980	0
$\gamma\,(h/6,b)*$	1300	726	726	-	556
$\gamma\,(-h/6,-b)*$	360	365	365	-	298
$\gamma\,(0,b/2)$	1060	-	521	-	-
$\gamma\,(0,b/3)$	-	488	-	-	442
$\gamma\,(0,2b/3)$	-	629	-	-	442

Table 3. Energies of the various planar faults (in $\mathrm{mJ\,m^{-2}}$) as calculated from the local minima of the five Functions A-E based on Equation (5). For comparison, published values of fault energies obtained from atomistic calculations and experimental measurements are also referenced.

Source	Material	γ_{SISF}	γ_{CISF}	γ_{APB}	γ_{SESF}	$\gamma_{\mathrm{CESF\text{-}1}}$	γ_{ISF}	γ_{ESF}
Function A	Ni_3Al	50	226	265	-	-	-	-
Function B*	Ni_3Al	62	196	276	74	268	-	-
Function C*	Ni_3Al	62	204	276	74	268	-	-
Function D	Ni	-	-	-	-	-	132	-
Function E*	Ni	-	-	-	-	-	137	140
Calculated energies								
Ref.[7]*	Ni_3Al	62	217	278	74	271	-	-
Ref.[10]	Ni_3Al	51	202	252	-	-	-	-
Ref.[36]	Ni_3Al	40	260	220	-	-	-	-
Ref.[6]	Ni_3Al	79	223	172	-	-	-	-
Ref.[37]	Ni_3Al	80	225	210	-	-	-	-
Ref.[38]	Ni_3Al	147	308	240	-	-	-	-
Measurements from TEM								
Ref.[39]	Ni_3Al	10±5	-	180±30	-	-	-	-
Ref.[40]	$Ni_{78}Al_{22}$	6±0.5	235±40	175±15	-	-	-	-
Ref.[41]	$Ni_{76}Al_{24}$	-	177±20	147±15	-	-	-	-